Structure and stability of an amorphous water–methane mixture produced by cold compression of methane hydrate

C. A. Tulk,[1,*] D. D. Klug,[2] J. J. Molaison,[1] A. M. dos Santos,[1] and N. Pradhan[1]

[1]*Chemical and Engineering Materials Division, Oak Ridge National Laboratory, Oak Ridge, Tennessee 37831, USA*
[2]*Steacie Institute for Molecular Sciences, National Research Council of Canada, Ottawa, ON, Canada K1A 0R6*

In a process similar to the formation of high-density amorphous ice, amorphous methane hydrate was formed by the pressure-induced collapse of crystalline methane clathrate at 32 kbar and 100 K. This produced a regular array of methane embedded within cavities in an amorphous water network. *In situ* annealing results in further densification into a more disordered and higher density amorphous state before crystallization into ice VIII and hexagonal clathrate. Whereas the very high-density amorphous form of pure water undergoes a glass transition near 130 K at low pressure and crystallizes over a broad pressure range at ∼160 K, the amorphous network of the water–methane binary system exhibits a region of metastability that persists up to 220 K between 15 and 40 kbar. It appears that in this system the connectivity of the water network exhibits sufficiently low mobility so as to inhibit the diffusion and phase separation of the constituents until 220 K, where the high-pressure ice VIII crystallization can occur. The structure of the amorphous form is studied by neutron diffraction and the hydration of methane in this disordered water network is more closely related to the small clathrate cage than the large.

PACS number(s): 62.50.−p, 64.70.pm, 61.20.−p, 64.70.D−

I. INTRODUCTION

Clathrate hydrates are icy materials consisting of a water lattice arranged to form cages that are occupied by guest atoms or molecules such as nitrogen, oxygen, carbon dioxide, noble gases, and small hydrocarbon molecules.[1,2] Perhaps the most studied among these is the cubic structure I (sI) gas hydrate containing methane. In this structure the water lattice is formed by two types of face-sharing cages, denoted as the 5^{12} small cage (comprised of 12 edge-shared five-member water rings) and the $5^{12}6^2$ large cage (comprised of 12 edge-shared five-member water rings and two edge-shared six-member water rings), and these cages are occupied by methane molecules. This type appears within the biosphere of the Earth as perhaps its largest reserve of natural gas, and when recovered, these gases create unwanted hydrate deposits and pose safety and flow problems for petroleum recovery and production. The methane–water system also plays a major role in physical processes of planetary and satellite bodies. Water ice is the most common mineralogical component of deep space bodies, along with light hydrocarbons, and plays a major role in planetary accretion.[3,4] The recent results from the Cassini-Huygens space probe of Saturn's largest moon Titan have shown vast quantities of methane in the solid, liquid, and gaseous forms on and near the surface.[5]

Terrestrial methane hydrate has been studied for many years, however, several fundamental questions remain unsolved. Perhaps chief among these are structural mechanisms by which clathrates form and decompose, and the molecular scale processes that allow water/ice to take-up and release gigatons of methane in the environment.[6] This requires an accurate understanding of the hydration structure of methane molecules in the noncrystalline state, that is, within a highly disordered network of water, be it liquid, on the disordered surface of ice, or in the glassy state.[7–10] Such experiments are difficult to conduct in the equilibrium liquid state because of the low solubility of methane in water (35 mg/l) and the need to use direct structural probes. However, it has been understood that clathrate hydrates will undergo a pressure-induced amorphization at temperatures near 77 K,[11–13] and this process and amorphous structure could be studied at the clathrate composition.

More fundamentally, as a tetrahedrally hydrogen bonded water network these materials should progress through structural transformations that resemble those of pure ice[14] and at low temperature, may undergo a similar volume collapse in the several tens of kilobar range to form an amorphous water matrix. We note here that pure hexagonal ice has a negative melting slope, and that pressure amorphization of methane hydrate may indicate that, under high pressure, methane hydrate has a negative melting slope as well. However, we caution that it is also possible that under high pressure an open structure such as structure I methane hydrate could collapse to an amorphous form, and not recrystallize, if the temperature is sufficiently low. Warming the amorphous mixture would likely produce high-pressure clathrate phases, or the system may phase separate to crystallize into pure high-pressure ice and clathrate. It is noted that pure amorphous ice recrystallizes upon *in situ* heating into a variety of high-pressure ices by first forming other, higher density, amorphous forms (e.g., the very high-density amorphous form known as VHDA).[15–18] This has led to the idea of glass transitions in these forms of amorphous ice between 130 and 160 K, and the existence of ultraviscous and deeply supercooled liquid states of water that can exhibit structural transformations between a high- and low-density state.[19,20] The recrystallization of these amorphous forms occurs slightly above 160 K, and the temperature drops off as the pressure is increased above 25 kbar.[21,22] Furthermore, while several clathrates have been shown to collapse upon pressurization at low temperature,[23,24] no detailed structural study of the resulting amorphous structures and the amorphous network rearrangement upon warming has been reported [e.g., measurement of a normalized structure factor function and Fourier inversion to provide a radial distribution function (rdf)].

In this paper, detailed structural studies of the collapse and annealing of an amorphous methane hydrate is described. The newly constructed high-pressure SNAP beamline at the Spallation Neutron Source at Oak Ridge National Laboratory has been used to collect *in situ* diffraction data, and molecular dynamics (MD) simulations have been used to help interpret the experimental results. Experimental neutron-weighted total structure factor functions [$S(Q)$] along with the atom-to-atom total and partial radial distribution functions (rdfs) are explored between the amorphization at 32 kbar, 39 kbar, and upon annealing between 100 and 220 K. Here methane approximates a sphere and weakly interacts with the water network. The water subnetwork in this binary system shows qualitative similarity with pure high-density amorphous ice in that the crystal is observed to first collapse into a dense amorphous structure, then exhibit network rearrangement upon annealing. However, unlike pure ice, the densified state exhibits a reduced level of intermediate-range order and a larger metastability field up to 220 K between 30 and 40 kbar, at which point the sample crystallizes. The extraction of partial rdfs from the MD simulations gives insight into the arrangement of methane molecules in the amorphous network, the relative stability of the large and small clathrate cages, and the hydration structure of methane deeply embedded in an amorphous water network.

II. EXPERIMENT AND SIMULATION

Fully deuterated methane hydrate, $CD_4 \bullet 6.26 D_2O$ (ratio refined from current data, see Sec. III), was synthesized by a technique outlined previously.[25] The samples were cold loaded (at 77 K) into a soft-metal-encapsulated (SME) single-toroid gasket made of a null scattering Ti-Zr alloy[26] and set into single-toroid cubic boron nitride anvils within a Paris-Edinburgh (PE) press on the SNAP instrument at the Spallation Neutron Source at Oak Ridge National Laboratory. A small load of about 7 ton was applied to the gasket, which generated enough pressure to seal the cell and stabilize the hydrate at room temperature. The sample was allowed to warm during transfer of the pressure cell to the instrument, and a preliminary spectra showed that the sample was sI hydrate and had not decomposed upon cell loading and warm-up. The sample was cooled to 100 K in the sI clathrate phase and then pressurized to 32 kbar (sample 1) and 39 kbar (sample 2). Both samples were then heated at 32 and 39 kbar until they crystallized. A third sample followed a similar path, however it was annealed just below 220 K and thus not crystallized but rather temperature quenched back to 100 K and decompressed to 15 kbar and annealed there to higher temperature until it crystallized. Neutron structure factor functions were obtained at several points along this path. These have been corrected for background, empty instrument, normalized to vanadium, and scaled at high-momentum transfer to the sum of the weighted scattering lengths of the constituent atoms, and the final $S(Q)$ is made to oscillate about one at high-momentum transfer. Pressures were determined by heating and recrystallizing each sample into ice VIII then using the calculated free volume of water from a Rietveld refinement and the ice equation of state. To aid in the interpretation of the data, MD simulations of the crystalline collapse were performed.

Isotropic *NPT* molecular dynamics simulations with the Nosé-Hoover barostat algorithm and the Melchionna *et al.* modification were performed on a periodically replicated $4 \times 4 \times 4$ cubic structure I clathrate hydrate supercell with 47.428 Å initial dimensions containing 2944 water molecules and 512 methane molecules employing the DL POLY code.[27] The thermostat and barostat relaxation times were 0.5 and 2.0 ps, respectively. The sI hydrate simulation cell was constructed with oxygen atoms placed at the crystallographiclly known sites in the $Pm\bar{3}n$ cubic unit cell and the positions of the water hydrogen atoms constrained by the Bernal-Fowler ice rules. The distribution of hydrogen atoms with a minimum dipole moment was chosen for the molecular dynamics simulations. The extended simple point charge (SPC/E) potential model[28] and the TIP4P/ice potential[29] were employed for water molecules and the Murad-Gubbins (MG) five-site potential model was used for methane.[30] Both models agree very well and only the TIP4P/ice results are shown in the figures reported in this paper. This combination reproduced the experimental data well. The Lorentz-Berthelot combination rules were used for obtaining Lennard-Jones potential parameters between unlike atom-type centers from the parameters for like atoms.

III. RESULTS

Diffraction data from the initial crystalline sI hydrate sample are shown in Fig. 1. Rietveld refinement of the crystalline data shows the sample is a single phase of sI hydrate with $a = 11.964$ Å, and large and small cage methane occupancies of 0.96 and 0.79, respectively. The onset of amorphization is initially indicated by the loss of Bragg peak intensity and formation of broad diffuse scattering at 32 kbar (Fig. 2). The corrected $S(Q)$ functions[31] from the amorphous sample 1 and sample 2 are shown in Fig. 2(a). Each data set was collected at constant PT conditions for 5 h, collection times were limited by the volume of liquid nitrogen available in the cryosystem. As mentioned above, heating and recrystallizing
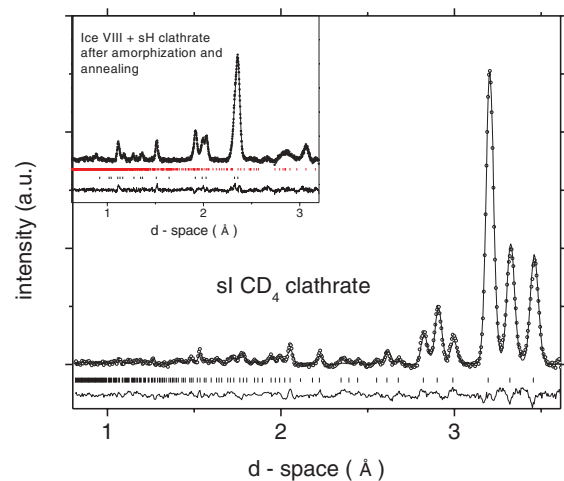

FIG. 1. (Color online) Diffraction data from the initial sample as loaded in the Paris-Edinburgh press, the initial sample is shown to be a single phase of sI clathrate. The inset shows the sample after *in situ* annealing and recrystallization into ice VIII and hexagonal clathrate at 32 kbar and 226 K.
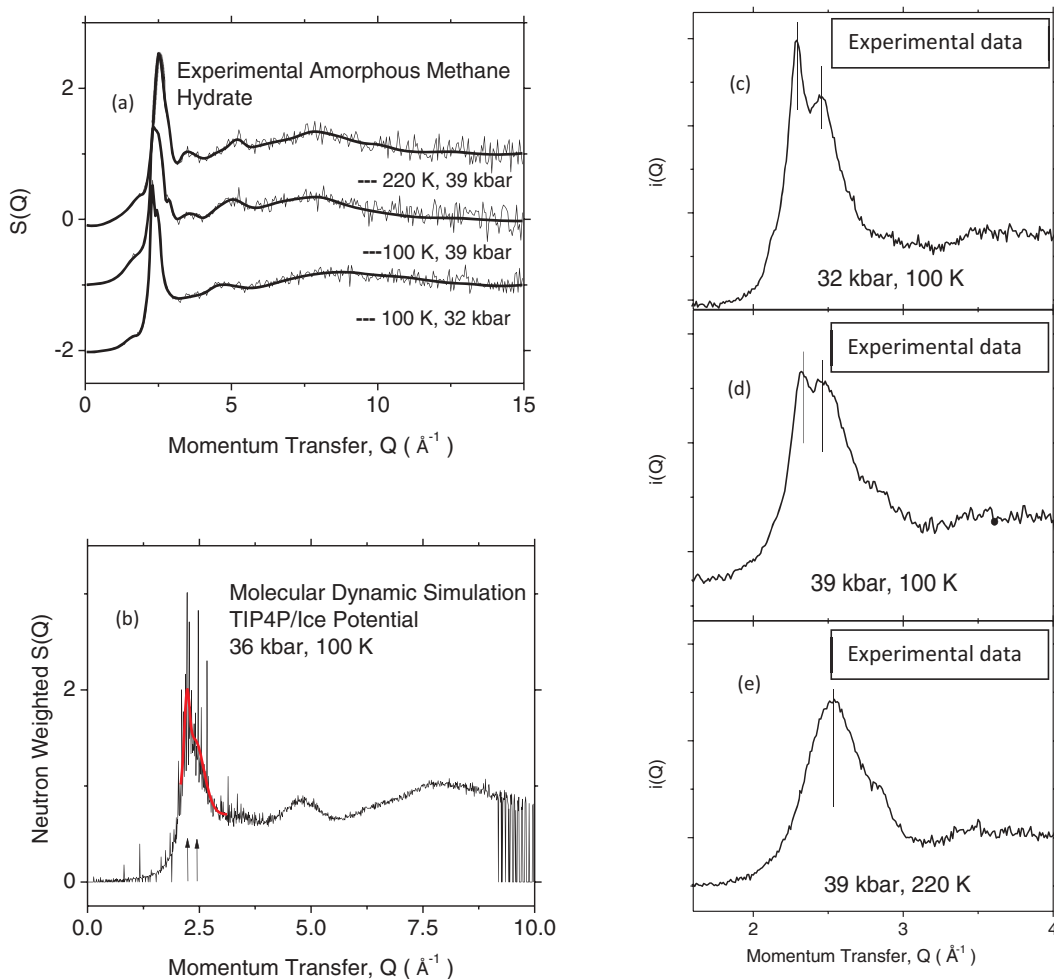
FIG. 2. (Color) The experimental (a) and simulated (b) structure factor functions of the collapsed amorphous clathrate forms. The experimental data has been corrected for background, empty instrument, normalized to vanadium, and scaled at high-momentum transfer to the sum of the weighted scattering lengths of the constituent atoms, and the final $S(Q)$ is made to oscillate about one at high Q. The vertical arrows in (b) indicate the positions of the two fitted peaks in the simulation. An expanded region in the vicinity of the first diffraction peak is shown in (c), (d), and (e) and illustrates the effect of annealing the sample at the conditions given, the solid vertical bars mark the peak positions.

each sample resulted in the formation of ice VIII, the pressure was then determined using the calculated free volume of water from a Rietveld refinement and the equation of state. The Fig. 1 inset shows diffraction data from a recrystallized sample. A slight error (<1 kbar) is introduced here.

The experimentally determined $S(Q)$ functions, shown in Fig. 2(a), are characterized by a dominant first diffraction peak (FDP) that first appears as a doublet at 32 kbar and 100 K. Expanded plots of this data in the region of the FDP are plotted with a finer data binning in Figs. 2(c)–2(e), where it is noted that as the pressure is increased from 32 to 39 kbar at 100 K, the splitting becomes less pronounced as the peaks merge. The relatively sharp nature of the FDP peak likely arises from a significant degree of intermediate range ordering (IRO) in the collapsed amorphous material. The two "strong" peaks would be indicative of two closely related length scales that are characteristic of the network, see discussion of simulated $S(Q)$ and $G(R)$ below. Furthermore, Fig. 2(a) also shows the data after the sample was warmed from 100 to 220 K at $P = 39$ kbar, here the main peak shifts to higher momentum

transfer and significantly broadens. The position of the FDP in an amorphous material, particularly ice, is a general indication of the density of the sample.[18,32] The larger Q value for the peak position indicates a greater density, and the width gives an indication of the radial extent of the ordering.[18] This behavior indicates an increasing density during annealing, a process that could be related to similar densification observed in amorphous ice but with an overall shortening in the radial extent of the IRO. Thus a *less ordered* very high-density amorphous (VHDA) form of methane clathrate has been formed.

To aid in understanding the experimental results the total, and partial, $S(Q)$ functions were calculated using MD simulations (a total of 263256 Q vectors were used). While the overall agreement with the experimentally determined $S(Q)$ is good, it appears that the simulation indicates a slightly less dense material than the experiment would suggest under similar conditions. As such, the peak splitting observed experimentally at 32 kbar is not reproduced in the simulation at that pressure, instead the peak splitting is reproduced at a slightly higher pressure of 36 kbar, with two peaks fitted at
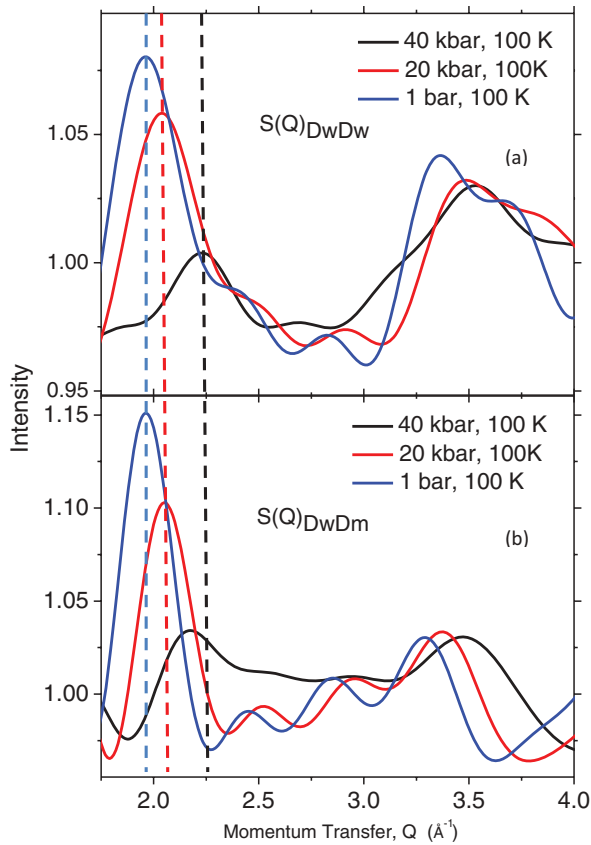
FIG. 3. (Color) The partial $S(Q)_{D_w-D_w}$ and $S(Q)_{D_w-D_m}$ function in (a) and (b), respectively, determined by molecular dynamic simulation. Here D_w denotes water deuterium and D_m denotes methane deuterium. Each panel shows data for 1 bar (sI crystalline), 20 kbar (sI crystalline), and 40 kbar (amorphous) forms. The vertical lines illustrate that the first peaks overlap in the crystalline phase but differ significantly in the amorphous phase.
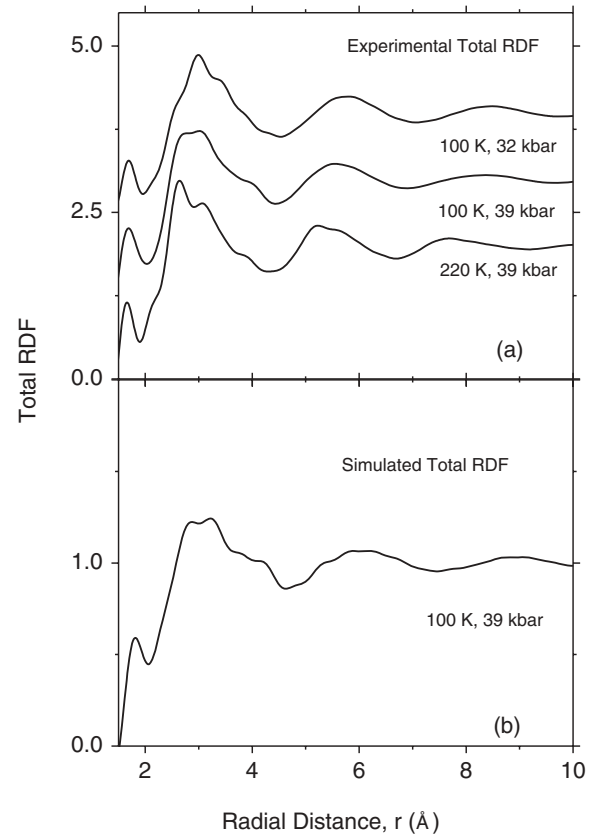

FIG. 4. Experimentally determined total radial distribution functions after initial collapse of the crystal at 100 K and 32 kbar, upon further compression to 39 kbar at 100 K, and upon annealing at 39 kbar to 220 K (a). The neutron weighted total radial distribution function determined by molecular dynamics simulation at 39 kbar at 100 K (b). The time scale of the MD simulations precluded modeling the annealing process.

momentum transfer values of $Q = 2.27$ and 2.51 Å, and this data is shown in Fig. 2(b), see the fitted red curve. The lower density produced in the simulation could result from the poorly understood methane–water potential function, particularly in the short-range region where the interaction is repulsive,[33] which dominates as the water cage collapses around the methane. The partial structure factor and radial distribution functions can now be extracted for any atom pair by labeling atom types in the MD simulation. In the neutron-weighted Faber-Ziman formalism[31] the dominant contributors to the $S(Q)$ are the D-D, and the D-O correlations. Furthermore, the D-D correlations are themselves composed of, in part, the D_w-D_w (where D_w water deuterium) correlations (28.6% of the total neutron weighting) and D_w-D_m (where D_m methane deuterium) correlations (19.9%). Together they make up almost 50% of the total neutron-weighted $S(Q)$. These partial $S(Q)$ functions, extracted from the MD simulation, are shown in Figs. 3(a) and 3(b) and help us understand how the host water network changes relative to the guest methane molecules as the crystal collapses. For the crystalline forms at 1 bar and 20 kbar, the FDP of these partials occur at the same momentum-transfer value. Although, with increasing pressure they simultaneously shift to higher Q value and drop in intensity, indicating an overall increase in the network density

and a slight decrease in IRO. However, after amorphization, from data at 40 kbar shown, it is clear that the FDP of the $S(Q)_{D_w-D_w}$ partial shifts toward higher Q value more rapidly than the FDP of the $S_{D_w-D_m}(Q)$ partial. A probable explanation for this behavior is that the water network is collapsing (or densifying) and becoming amorphous but that water–methane repulsion retains a form of cavity structure around methane, which is hence densifying at a slower rate. This idea can explain the split peak observed in the experimental data and could explain why the network in some clathrate "springs" back to the crystalline form upon decompression. Annealing this residual structure out may allow the amorphous sample to be recovered.

The neutron-weighted total rdfs can be determined from Fourier inversion of the experimental $S(Q)$ data and directly from analysis of the atomic positions in the MD simulation box, these data are shown in Figs. 4(a) and 4(b), respectively. Again, the agreement between the simulation and experiment in this P-T range is remarkable (but as mentioned, the simulation gives a slightly less-dense structure). Upon increasing the pressure, the first peak at about 1.75 Å [Fig. 4(a)], which arises from the intermolecular water D$\cdots$O hydrogen bond, is observed to be almost incompressible over this pressure range, and the correlations at greater radial distance move
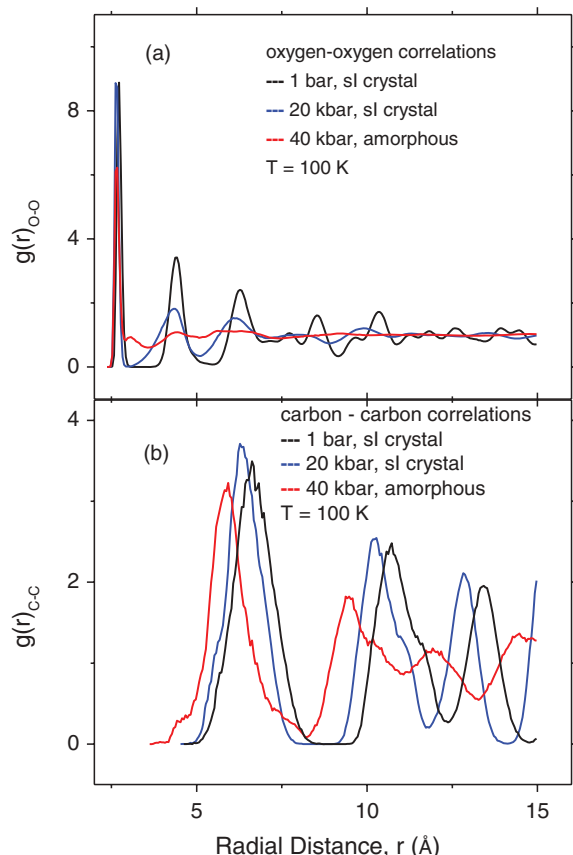
FIG. 5. (Color) The partial oxygen-to-oxygen radial distribution function $g(r)_{O-O}$ determined from the MD simulation (a). These data show that after collapse, at 40 kbar, the water network exhibits only limited short-range order. The partial carbon-to-carbon radial distribution function $g(r)_{C-C}$ determined from MD simulation (b). Even in the amorphous form there remains a significant degree of intermediate range ordering of methane within the amorphous water network.

inward. This network "folding" is thus responsible for the increasing density with pressure and annealing. The partial radial distribution functions can also be extracted from the MD simulation. The oxygen–oxygen partials $g(r)_{O-O}$ determined from the simulation are shown in Fig. 5(a) at 1 bar (crystalline), 20 kbar (crystalline), and 40 kbar (amorphous). The nearest-neighbor shell is observed to be at $r = 2.74$ Å and, as expected, only compresses slightly with pressure. At 20 kbar, the long-range correlations of the oxygen are still present but with broader peaks, indicating the water network, though still crystalline, is slightly less ordered. After collapse at 40 kbar the first oxygen shell is well defined at $r = 2.66$ Å, but the extended IRO has essentially vanished beyond $r = 4$ Å. The water subnetwork has become amorphous. Additionally, the slight increase at $r = 3$ Å shows second-nearest neighbor oxygen atoms are approaching the first O–O coordination shell, similar to the higher density amorphous ices.

Likewise, the partial $g(r)_{C-C}$, determined again from the simulation, is plotted in Fig. 5(b) and gives the distance from methane center to methane center. In this plot, the large and small cages are not distinguished, and at 1 bar and 20 kbar the nearest neighbor methane molecules form one peak centered at

6.63 and 6.34 Å, respectively. This approximates the average distance from cage center to cage center and shows the regular array of methane molecules embedded within the crystal network. At 40 kbar, when the water network is amorphous, a significant level of short range order still exists in the methane–methane substructure to at least $r = 16$ Å. Thus, at least over the intermediate range, a regular array of methane is embedded in the amorphous water network.

Insight into the process of water-cage collapse around methane can be gained by further analysis of the simulation results to extract the carbon to water-deuterium partial rdf, $g(r)_{C-D_w}$. These are plotted for both the large and small clathrate cages in Figs. 6(a) 1 bar, 6(b) 20 kbar, and 6(c) 40 kbar. Each plot overlays the $g(r)_{CS-D_w}$ and $g(r)_{CL-D_w}$, where CS and CL are the carbon atoms in the small and large cage, respectively. At 1 bar and 20 kbar the first peak in the rdfs represents the average distance from the carbon atom to the deuterium in the cage water molecule. This distance is characteristic of each cage type in the crystalline form (note that the methane may not be located at the center of the cage). The carbon-to-deuterium distance decreases more rapidly with pressure for the large cage, note the peak shifts from 3.57 Å (small) and 3.87 Å (large) at 1 bar [Fig. 6(a)] to 3.44 Å (small) and 3.62 Å (large) at 20 kbar [Fig. 6(b)]. The MD data in Fig. 5(a) give the O-O distances and allow the average O-O-O angle to be determined. In the crystal this angle changes from 107.4° at 1 bar to 110.7° at 20 kbar as these cages compress. Furthermore, the data from the amorphous form at 40 kbar [Fig. 6(c)] show that the carbon-to-water deuterium distance is nearly the same for both types of cage. Indeed the similarities in these rdfs extend to the level of intermediate range ordering, around $r = 10$ Å, thus, there appears to be little structural difference between the cavity types in the amorphous form. This gives an indication of the repulsive part of the methane water potential, however, such an analysis is not within the scope of the current paper and is left for a later study.

To finish, heating the sample above 220 K results in recrystallization and it is possible to estimate the extent of the movement of methane through the amorphous network during phase separation (and crystallization) of ice VIII, Fig. 1 inset, and it is interesting to compare the crystallization temperature versus pressure curve of pure ice with the crystallization temperature versus pressure curve of the binary water–methane mixture. Taking the experimental data and the insight gained from simulation, it is clear that the process of transforming the sI clathrate to the dense high-pressure ice VIII structure involves the methane effectively coming out of the amorphous "solid solution" to leave regions of water large enough to nucleate and grow the bulk forms of pure crystalline ice. Assuming that the "liquid-like" nature of the water network upon annealing near 225 K relieves pressure-induced stresses, the ice particle size can be estimated using the Scherrer formula and peak width parameters from the Rietveld refinement. This would put an upper bound on the diffusion length of the methane through the water network prior to crystallization (however, the methane could have diffused a shorter distance thus giving the overall ice VIII structure but with disrupted order and a broadening of diffraction peaks). A standard nickel pellet was used to parametrize the instrumental linewidths, particle size broadening then gives $\sigma_2^2 = 33.3$, and using the
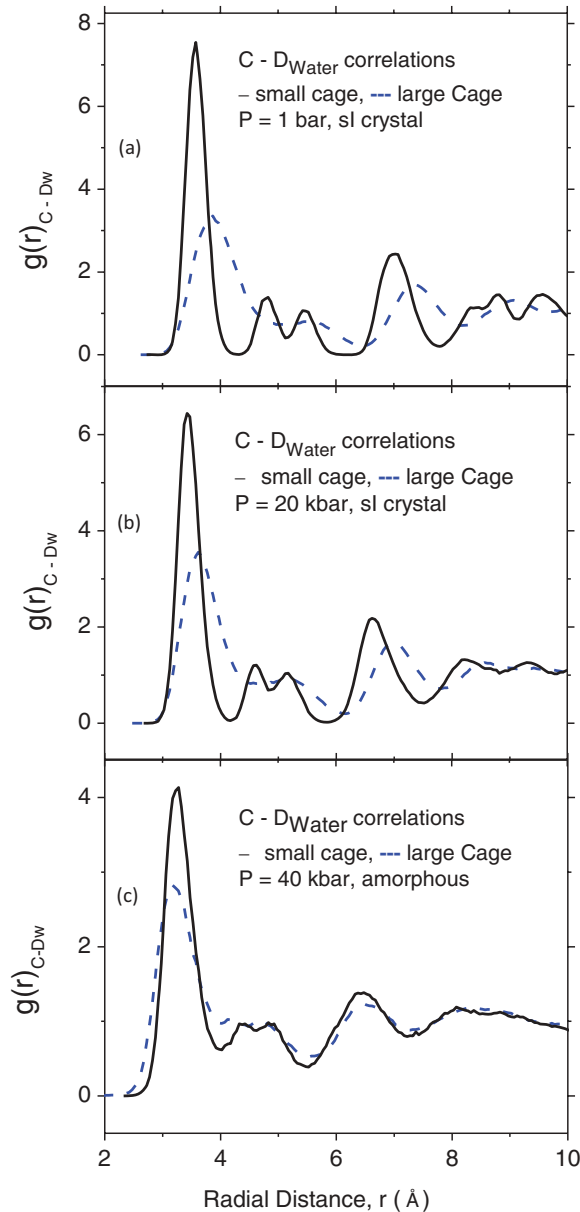
FIG. 6. (Color online) The partial carbon-to-water deuterium radial distribution functions $g(r)_{C-D_w}$, as determined by the MD simulation, for both the small and large cage. Here C represents the carbon atom of the methane molecule and D_w represents the deuterium atoms of the water molecules. Each panel shows partials from both small and large cages for 1 bar (a), 20 kbar (b), and 40 kbar (c).
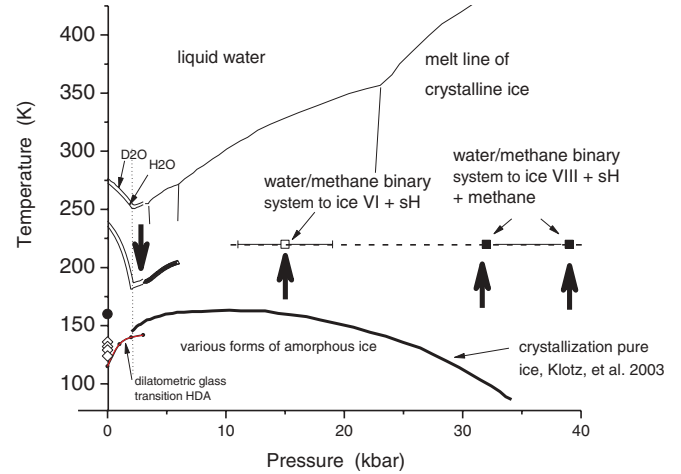

FIG. 7. (Color) Experimental data showing the stability limits of various forms of water. The (dilatometric) glass transformations (red curve) and crystallization data (heavy black curve) of various forms of high-density amorphous ice over a broad pressure range. The reported glass transition temperatures (open diamonds) and crystallization temperature (solid circle) of low-density amorphous ice (LDA) at 1 bar. The melt line of both H_2O and D_2O are plotted below 3 kbar. The supercooling limit of liquid water upon cooling for both H_2O and D_2O are also plotted below 3 kbar (the arrow pointing downward indicates crystallization upon cooling). The extension of this curve up to 6 kbar is not experimental data but is taken to be parallel to the crystalline melt line over this pressure range. Also plotted here are the crystallization data for a binary mixture of amorphous water and methane from the current experiments (squares connected by dashed curve and the three arrows pointing upward indicate crystallization upon heating). The solid black squares are samples that crystallized into ice VIII, methane, and hexagonal hydrate, and the open square is the sample that crystallized into ice VI and hexagonal hydrate. These samples transformed from an amorphous binary methane water mixture to crystalline ice VIII + sH hydrate over 2 h between 220 and 225 K. Analysis of the ice VIII cluster size indicates the methane could have diffused a maximum of 116 Å through the water network at temperatures near 220 K.

GSAS protocol gives a particle size of 232.2 and 337 Å at 32 and 39 kbar, respectively. On average, methane would have moved half this distance to clear this volume, and over the 2 h anneal between 220 and 225 K the diffusion coefficients of methane through the water network of 9.34×10^{-17} and 3.92×10^{-16} cm^2/s at 32 and 39 kbar, respectively. This is lower than the self-diffusion of water in crystalline ice Ih. Finally, the crystallization curves of pure amorphous water, the melt line of crystalline ice, and the crystallization curve of binary methane–water system are shown in Fig. 7, along with the stability limit of liquid water upon supercooling, and the measured glass transition temperatures of pure water

upon heating. These data show the difference in the stability of the pure water network and a water network loaded with hydrophobic methane molecules.

IV. DISCUSSION

Upon low-temperature pressurization of methane clathrate the crystal structure collapses into an amorphous water network containing methane molecules. Analysis of the experimental data and MD simulations indicates that, upon collapse, the ice network becomes amorphous and the position of the methane molecules remain highly correlated within the water network. After the collapse, the methane molecules from the large and small clathrate cages have a similar hydration structure, which at the local level bears a resemblance to the small 5^{12} crystalline cage. The appearance of a doublet in $S(Q)$ for the amorphous form indicates two length scales that are characteristic of the network IRO. Given the neutron weighting factors of the $S(Q)_{D_w-D_w}$ and the $S(Q)_{D_m-D_w}$ partials, the characteristic length scales can likely be attributed to those

correlations of the water subnetwork, and those between the water–methane subnetwork.

At 32 and 39 kbar the overall amorphous structure is observed to further densify upon warming into a more disordered state, which is here termed a VHDA form that exhibits a large field of metastability before crystallizing into ice VIII and hexagonal clathrate at 220 K. This is much greater than the metastability field of pure amorphous water, which crystallizes at much lower pressure and temperature.[21] It seems that mobility of the methane bearing water network below 220 K is too low to allow the effective phase separation of methane and water that is required for crystalline ice VIII to form and grow. Enclathrated methane therefore appears to increase the metastability field of the amorphous network. The lower pressure behavior of the amorphous water–methane system remains to be studied. As such, this work has consequences for current ideas on the hydration structure of methane deeply embedded in a disordered water network and can give insight into the processes of hydrate formation and decomposition.

While noting that the features of the oxygen–oxygen partial rdf of the water subnetwork here does bear a resemblance to that determined for pure high-density amorphous water by Saitta *et al.*,[34] and, to the extent that the pure ice system and the water subnetwork in the binary water–methane system can be compared, the crystallization data of supercooled water, the thermal and dilotometric[35] glass transitions data of noncrystalline ice, and the current data from amorphous methane–water mixtures can be plotted together (Fig. 7). As such it can be seen that heating pure amorphous water above about 160 K is interrupted by crystallization to a high-pressure crystalline ice phase over a broad pressure range,[21] and as a result water cannot be studied continuously from the noncrystalline solid to the stable liquid. However, the addition of methane to the amorphous water network forms a binary system that inhibits the formation of crystalline ice and effectively allows the amorphous water subnetwork to remain amorphous to greater temperature. The crystallization into ice VIII observed here (with the particle dimensions estimated above) shows the phase separation of methane from the amorphous water network occurs, on an experimental time scale, just above 220 K. This temperature range overlaps with that of the reported fragile-to-strong transition in pure liquid water on cooling.[19] In addition, this shows that the stability limit of this noncrystalline binary water–methane network upon heating lies near a reasonable extension of the stability limit of pure liquid water upon supercooling, and near the "fictive" temperature where the structure of equilibrium water becomes frozen (glassy) upon rapid cooling.[36,37]

ACKNOWLEDGMENTS

---

[*]Corresponding author: tulkca@ornl.gov

[1]G. A. Jeffrey, in *Comprehensive Supramolecular Chemistry*, edited by J. L. Atwood, J. E. D. Davies, D. D. MacNicol, F. Vogtle, and J. M. Lehn (Pergamon, Elsevier Science, New York, 1996), Vol. 6, Chap. 23.

[2]J. A. Ripmeester, C. I. Ratcliffe, D. D. Klug, and J. S. Tse, Ann. N.Y. Acad. Sci. **715**, 161 (1994).

[3]A. D. Fortes and M. Choukroun, Sci. Rev. **153**, 185 (2010).

[4]A. Léger *et al.*, Icarus **169**, 499 (2004).

[5]R. Jaumann *et al.*, in *Titan from Cassini-Huygens*, edited by R. H. Brown, J.-P. Lebreton, and J. Hunter Waite (Springer, New York, 2009), pp. 75–140.

[6]A. Milkov, Earth-Sci. Rev. **66**, 183 (2004).

[7]P. Buchanan *et al.*, J. Chem. Phys. **123**, 164507 (2005).

[8]H. Thompson *et al.*, J. Chem. Phys. **124**, 164508 (2006).

[9]J. S. Tse and D. D. Klug, J. Supramol. Chem. **2**, 467 (2002).

[10]A. Hallbrucker, J. Chem. Soc. Faraday Trans. **90**, 293 (1994).

[11]Y. P. Handa, J. S. Tse, D. D. Klug, and E. Whalley, J. Chem. Phys. **94**, 623 (1991).

[12]Y. Suzuki, Phys. Rev. B **70**, 172108 (2004).

[13]H. Tanaka and Y. Amano, Mol. Phys. **100**, 2183 (2009).

[14]O. Mishima, L. D. Calvert, and E. Whalley, Nature (London) **310**, 393 (1984).

[15]T. Loerting, C. Salzmann, I. Kohl, E. Mayer, and A. Hallbrucker, Phys. Chem. Chem. Phys. **3**, 5355 (2001).

[16]C. G. Salzmann *et al.*, Phys. Chem. Chem. Phys. **8**, 386 (2006).

[17]C. G. Salzmann, E. Mayer, and A. Hallbrucker, Phys. Chem. Chem. Phys. **6**, 5156 (2004).

[18]C. A. Tulk, R. Hart, D. D. Klug, C. J. Benmore, and J. Neuefeind, Phys. Rev. Lett. **97**, 115503 (2006).

[19]P. G. Debenedetti, J. Phys.: Condens. Matter **15**, R1669 (2003).

[20]O. Mishima, J. Chem. Phys. **133**, 144503 (2010).

[21]S. Klotz, G. Hamel, J. S. Loveday, R. J. Nelmes, and M. Guthrie, Z. Kristallogr. **218**, 117 (2003).

[22]R. J. Nelmes, J. S. Loveday, T. Strassle, C. L. Bull, M. Guthrie, G. Hamel, and S. Klotz, Nat. Phys. **2**, 414 (2006).

[23]Y. P. Handa, J. S. Tse, D. D. Klug, and E. Whalley, J. Chem. Phys. **94**, 623 (1991).

[24]M. Bauer *et al.*, Phys. Chem. Chem. Phys. **13**, 2167 (2011).

[25]Y. P. Handa, J. Chem. Thermodyn. **18**, 891 (1986).

[26]W. G. Marshall and D. J. Francis, J. Appl. Crystallogr. **35**, 122 (2002).

[27]T. R. Forester and W. Smith, Eds., DLPOLY 2.14, CCLRC, Daresbury Laboratory, 1995.

[28]H. J. C. Berendsen, J. R. Grigera, and T. P. Straatsma, J. Phys. Chem. **91**, 6269 (1987).

[29]J. L. F. Abascal, E. Sanz, R. García Fernández, and C. Vega, J. Chem. Phys. **122**, 234511 (2005).

[30]S. Murad and K. E. Gubbins, in *Computer Modeling of Matter*, edited by P. Lykos (American Chemical Society, Washington, DC, 1978), Vol. 62.

[31]T. E. Faber and J. M. Ziman, Philos. Mag. **11**, 153 (1965).

[32] C. J. Benmore, R. T. Hart, Q. Mei, D. L. Price, J. Yarger, C. A. Tulk, and D. D. Klug, Phys. Rev. B **72**, 132201 (2005).

[33] C. A. Tulk, D. D. Klug, A. M. dos Santos, G. Karotis, M. Guthrie, J. J. Molaison, and N. Pradhan, J. Chem. Phys. **136**, 054502 (2012).

[34] A. M. Saitta, T. Sträsle, and S. Klotz, J. Chem. Phys. B **110**, 3595 (2006).

[35] M. Seidl, M. S. Elsaesser, K. Winkel, G. Zifferer, E. Mayer, and T. Loerting, Phys. Rev. B **83**, 100201 (2011).

[36] G. Fleissner, A. Hallbrucker, and E. Mayer, J. Chem. Phys. B **102**, 6239 (1998).

[37] D. D. Klug, C. A. Tulk, E. C. Svensson, and C.-K. Loong, Phys. Rev. Lett. **83**, 2584 (1999).